An Analytical Model for CO_2 Forcing, Part II: State-Dependence and Spatial Variations

Nadir Jeevanjee*, Jacob T. Seeley†, David Paynter‡, and Stephan Fueglistaler§

Princeton University, Princeton, New Jersey

Corresponding author address: Nadir Jeevanjee, Geosciences Department, Princeton University, Princeton NJ 08544

E-mail: nadirj@princeton.edu

†Harvard University Center for the Environment, Cambridge MA

‡NOAA/GFDL, Princeton NJ

§Geosciences Department, Princeton University, Princeton NJ 08544

ABSTRACT

Clear-sky CO_2 forcing is known to vary significantly over the globe, but the state dependence which controls this is not well understood. Here we extend the formalism of Seeley et al. (2020) to obtain a quantitatively accurate analytical model for spatially-varying CO_2 forcing, which depends only on surface and stratospheric temperatures as well as column relative humidity. This model shows that CO_2 forcing is primarily governed by surface-stratosphere temperature contrast, with the corollary that the meridional gradient in CO_2 forcing is largely due to the meridional surface temperature gradient. The presence of H_2O modulates this forcing gradient, however, by substantially reducing the forcing in the tropics, as well as introducing forcing variations due to spatially-varying column relative humidity.

1. Introduction

Changes in the Earth's CO_2 greenhouse effect (i.e. CO_2 radiative forcing) have been a primary driver of past and present changes in Earth's climate, and are well simulated by state-of-the-art radiation codes for a given atmospheric state (e.g. Mlynczak et al. 2016; Pincus et al. 2015; Oreopoulos et al. 2012; Forster et al. 2011). While this accuracy is critical for credible climate simulation and has thus been a priority for radiation research, less emphasis has been placed on an intuitive understanding of CO_2 forcing and its dependence on atmospheric state variables and hence geography or climate. For instance, zonally averaged clear-sky CO_2 forcing exhibits a marked meridional gradient (e.g. Huang et al. 2016), but what causes this? Answering such questions seems particularly worthwhile given that CO_2 forcing is such a basic quantity in climate science.

While not very well understood, this dependence of CO_2 forcing on atmospheric state (and the ensuing spatial heterogeneity of CO_2 forcing) has been known for some time and has been variously attributed to heterogeneities in surface temperature, lapse rate, water vapor, and cloudiness (Zhang and Huang 2014; Byrne and Goldblatt 2014; Govindasamy and Caldeira 2000; Shine and Forster 1999; Myhre and Stordal 1997; Kiehl and Briegleb 1993). Such studies have typically still emphasized global mean forcing, however, and any attribution of the spatial structure has been only qualitative. Recently, however, Huang et al. (2016) (hereafter H16) studied the spatial heterogeneity of CO_2 forcing, and developed a highly accurate multilinear regression model for CO_2 forcing which identified the temperature lapse rate as the most important single predictor for clear-sky CO_2 forcing, followed by water vapor path. While these results point the way towards understanding, such regression models cannot tell us whether their predictors have a fundamental significance or are simply correlated with the state variables that really matter. Furthermore,

such models offer limited mechanistic insight beyond that already required to sensibly choose predictors.

Here we attempt to push our understanding further by developing a first-principles, analytical model for spatially varying clear-sky CO_2 forcing. The analytical model builds on the one presented in the companion paper Seeley et al. (2020) (as well as that found in Wilson and Gea-Banacloche (2012)) by accounting for H_2O overlap. Our analytical model is able to emulate the global distribution of clear-sky radiative forcing produced by benchmark radiation codes, and the simplicity of the model allows us to identify and understand the driving factors behind the geographical distribution of this forcing.

We begin in Section 2 by heuristically deriving the analytical model of Seeley et al. (2020), specialized to the 500-850 cm^{-1} spectral region. In Section 4 we use this model to compute the global distribution of CO_2 forcing in the absence of H_2O for a snapshot of GCM output, comparing also to a global benchmark radiation calculation. In this CO_2-only case, the analytical model shows that CO_2 forcing arises from surface-stratosphere temperature contrast, and thus that meridional gradients in CO_2 forcing are due almost entirely to the meridional surface temperature gradient. In Section 5 we extend the analytical model to account for H_2O overlap. We again compute global forcing distributions using both the analytical model and a benchmark code, and find that H_2O overlap strongly modulates the meridional gradient in CO_2 forcing, by substantially reducing the forcing in the tropics as well as introducing variations from spatially-varying column relative humidity.

This work focuses on the instantaneous, top-of atmosphere (TOA), clear-sky forcing. Thus, the effects of clouds (e.g. H16, Merlis 2015) as well as stratospheric adjustment (e.g. H16, Zhang and Huang 2014; Stuber et al. 2001; Hansen et al. 1997; Houghton et al. 1994) are largely neglected. Furthermore, the difference between instantaneous TOA forcing and instantaneous tropopause

forcing must be kept in mind, as the former underestimates and the latter overestimates the adjusted forcing, by as much as 40%. (e.g. H16, Zhang and Huang 2014). Consequently, the global mean instantaneous TOA forcing values shown here will be significantly lower than the somewhat canonical *adjusted* value of 3.7 $\mathrm{W/m^2}$ per doubling (Ramaswamy et al. 2001; Myhre et al. 1998). The effects of clouds and stratospheric adjustment on CO_2 forcing are discussed further in Section 7, and an extension of this model to instantaneous tropopause forcing is given in Seeley et al. (2020).

2. Theory

In this section we heuristically derive an analytical model for (clear-sky, instantaneous, TOA) CO_2 forcing, where CO_2 is the only radiatively active species (i.e. 'CO_2-only'). This model is very similar to that from Seeley et al. (2020), except we determine our parameters somewhat differently and we treat the 500-850 $\mathrm{cm^{-1}}$ spectral region only. This spectral region is centered roughly around the absorption peak at 667 $\mathrm{cm^{-1}}$, and we will refer to it heuristically as the '667 $\mathrm{cm^{-1}}$ band', or simply 'the CO_2 band'.

We begin with a parameterization of the spectrum of CO_2 mass absorption coefficients in the 667 $\mathrm{cm^{-1}}$ band, evaluated at a reference pressure and temperature of $p_{\mathrm{ref}} = 100$ hPa and $T_{\mathrm{ref}} = 250$ K, as

$$\kappa_{\mathrm{ref}}(\widetilde{\nu}) = \kappa_0 \exp\left(-\frac{|\widetilde{\nu} - \widetilde{\nu}_0|}{l}\right) \tag{1}$$

where $\widetilde{\nu}$ denotes wavenumber (following Petty 2006; Houghton 2002; Thomas and Stamnes 2002), $\widetilde{\nu}_0 = 667.5$ $\mathrm{cm^{-1}}$, $\kappa_0 \approx 60$ $\mathrm{m^2/kg}$ is a representative mass absorption coefficient at $\widetilde{\nu}_0$, and the 'spectroscopic decay' parameter $l = 10.4$ $\mathrm{cm^{-1}}$ sets the rate at which κ_{ref} declines (exponentially) away from band center. The parameters l and κ_0 may be obtained by fitting (1) to a reference absorption spectrum produced by a line-by-line (LBL) radiation code, but the parameters turn out

to depend somewhat on details of the fit (e.g. Seeley et al. 2020; Jeevanjee and Fueglistaler 2020b; Wilson and Gea-Banacloche 2012). Instead, we opt to determine these parameters via optimization as described in Section 3.

We now write down the optical depth $\tau_{\widetilde{\nu}}$ at a given wavenumber $\widetilde{\nu}$, with pressure broadening but without temperature scaling (equivalent to setting $n = 1$ in Eqn. (3) of Seeley et al. 2020):

$$\tau_{\widetilde{\nu}} \;=\; D\kappa_{\text{ref}}(\widetilde{\nu}) \int_0^p \frac{q\,p'}{g p_{\text{ref}}} dp' \;=\; \frac{D\kappa_{\text{ref}}(\widetilde{\nu}) q}{2g} \frac{p^2}{p_{\text{ref}}} \,. \tag{2}$$

Here q is the CO_2 specific concentration and $D = 1.5$ is a 2-stream diffusion coefficient (e.g. Clough et al. 1992). Rather than use this to solve the radiative transfer equations, however, we instead employ the 'emission level' approximation wherein we approximate the emission to space from CO_2 at a given wavenumber as occurring entirely at a certain emission level τ_{em}. (The emission level approximation is discussed further in Appendix B.) Setting $\tau_{\widetilde{\nu}} = \tau_{\text{em}}$ in (2) and combining with Eqn. (1) then yields the 'emission pressure' $p_{\text{em}}(\widetilde{\nu}, q)$:

$$p_{\text{em}}(\widetilde{\nu}, q) \;=\; \underbrace{\sqrt{\frac{2\tau_{\text{em}} g p_{\text{ref}}}{Dq\kappa_0}}}_{p_0(q)} \exp\left(-\frac{|\widetilde{\nu} - \widetilde{\nu}_0|}{2l} \right) \,. \tag{3}$$

The pressure $p_0(q) \equiv p_{\text{em}}(\widetilde{\nu}_0, q)$ is an effective emission pressure at the center of the CO_2 band. We show in Appendix B that a suitable CO_2 emission level for our purposes is $\tau_{\text{em}}^{CO_2} = 0.5$. With this input, and for $q = 280$ ppmv, we find $p_0 = 16$ hPa, well into the stratosphere. [In reality, of course, the absorption coefficients and hence emission pressures near the center of the CO_2 band are highly wavenumber dependent (e.g. Coakley Jr. and Yang 2014) and can reach pressures lower than 16 hPa. Thus the notions of a 'representative' peak absorption coefficient κ_0 or an 'effective' peak emission pressure p_0 are most definitely idealizations, but ones which will prove useful.]

Equation (3) can also be inverted for the wavenumbers $\widetilde{\nu}_{\text{em}}$ emitting at a given p and q :

$$\widetilde{\nu}_{\text{em}}^{\pm}(p, q) \;=\; \widetilde{\nu}_0 \;\pm\; l \ln\left(\frac{Dq\kappa_0 p^2}{2\tau_{\text{em}} g p_{\text{ref}}} \right) \,. \tag{4}$$

Note the logarithmic dependence of $\widetilde{\nu}_{\rm em}$ on q in this equation.

Figure 1a plots $p_{\rm em}(\widetilde{\nu})$ from Eqn. (3) for an initial CO_2 concentration $q_{\rm i} = .000280 \times 44/29 = .000425$ kg/kg, and for a final CO_2 concentration of $q_{\rm f} = 4q_{\rm i}$. Using a logarithmic axis for $p_{\rm em}(\widetilde{\nu})$ yields triangles in the $\widetilde{\nu} - p$ plane, with the triangle in the $q_{\rm f}$ case being taller and wider than that from $q_{\rm i}$. Figure 1b also shows $p_{\rm em}(\widetilde{\nu})$ but as calculated with a benchmark line-by-line code (see calculation details in Section 3). To first order, the triangle picture is a reasonable approximation to the benchmark result.

The simplicity of the idealized $p_{\rm em}(\widetilde{\nu})$ triangles in Fig. 1a allows for a heuristic derivation of the CO_2 forcing $\mathscr{F}$ (defined as minus the difference in outgoing longwave between the $q_{\rm f}$ and $q_{\rm i}$ cases), as follows. Each orange point on the $q_{\rm i}$ curve has a corresponding point on the orange $q_{\rm f}$ curve at the same height, and thus both points have the same temperature and thus emission to space (neglecting variations in Planck function across these small spectral intervals). The orange portions of the two curves thus make identical contributions to the outgoing longwave, and thus can be neglected in calculating $\mathscr{F}$.[1] There are thus only two contributions to $\mathscr{F}$: one is the addition of new stratospheric emission from the $q_{\rm f}$ curve above $p_0(q_{\rm i})$ (dashed green), and the other is the loss of surface emission at wavelengths which were previously optically thin (solid red). In other words, the forcing is simply a swap of surface emission for stratospheric emission. This new stratospheric emission is of course what cools the stratosphere in response to increased CO_2, and it emanates from a characteristic stratospheric temperature

$$T_{\rm strat} \equiv T\left(\sqrt{p_0(q_{\rm i})p_0(q_{\rm f})}\right) \tag{5}$$

where we take a geometric mean of the initial and final p_0 values to account for the roughly logarithmic dependence of T on p. For given surface and stratospheric temperatures $T_{\rm s}$ and $T_{\rm strat}$,

[1] To the extent that the cooling-to-space approximation holds (Jeevanjee and Fueglistaler 2020a), this is consistent with a negligible change in tropospheric heating rate under CO_2 doubling for the CO_2-only case, as seen in e.g. Sejas et al. (2016) (their Fig. 6c).

then, their contributions to the forcing can be estimated once we know the spectral width $\Delta\widetilde{\nu}$ over which these contributions are made (Fig. 1a). Using (4), we find that this effective widening of the CO_2 band from changing q_i to q_f is given by

$$\Delta\widetilde{\nu} = l \ln\left(\frac{q_f}{q_i}\right) . \tag{6}$$

The logarithmic dependence of $\Delta\widetilde{\nu}$ on q, which follows from (4), arises because $\tau_{\widetilde{\nu}} \sim q e^{-|\widetilde{\nu}-\widetilde{\nu}_0|/l}$, so for fixed p and $\tau_{\widetilde{\nu}} = \tau_{em}$, an arithmetic change in $\widetilde{\nu}$ (which causes a uniform widening of the CO_2 band) requires a *geometric* increase in q, because the $\widetilde{\nu}$-dependence of $\tau_{\widetilde{\nu}}$ is exponential. Since the forcing is proportional to $\Delta\widetilde{\nu}$ (Fig. 1a), this is then the origin of the logarithmic scaling of CO_2 forcing, as derived more rigorously in Seeley et al. (2020). Also note that the overall scale of $\Delta\widetilde{\nu}$ is governed by the spectroscopic decay parameter l, which governed the exponential decay of $\kappa_{ref}(\widetilde{\nu})$ in Eqn. (1). Such a dual role for the spectroscopic decay parameter also occurs in the context of radiative cooling (Jeevanjee and Fueglistaler 2020b).

Returning to our derivation, if we denote the hemispherically integrated Planck function by $\pi B(\widetilde{\nu}, T)$, units of $\mathrm{W/m^2/cm^{-1}}$, we can thus estimate $\mathscr{F}$ in this CO_2-only case as

$$\mathscr{F} = 2l \ln\left(\frac{q_f}{q_i}\right) [\, \pi B(\widetilde{\nu}_0, T_s) - \pi B(\widetilde{\nu}_0, T_{strat}) \,] \qquad (CO_2\text{-only}) . \tag{7}$$

This expression is equivalent to Eqn. (25) of Wilson and Gea-Banacloche (2012), as well as Eqn. (10) of Seeley et al. (2020) specialized to the 667 $\mathrm{cm^{-1}}$ band. Note that besides the initial and final CO_2 concentrations, the only atmospheric state variables appearing in Eqn. (7) are T_s and T_{strat}. This suggests that CO_2 forcing is primarily governed by the the surface-stratosphere temperature contrast $T_s - T_{strat}$, and that the tropospheric lapse rates emphasized by H16 are only a proxy for $T_s - T_{strat}$, insofar as their vertical integral determines $T_s - T_{strat}$. This further suggests that *local* values of the tropospheric lapse rate are not relevant for CO_2 forcing, a prediction verified in

Seeley et al. (2020). Further physical implications of Eqn. (7) will be discussed when we study spatial variations of CO_2 forcing in Section 4.

3. Line-by-line calculations and parameter optimization

In the remainder of this paper we will test Eqn. (7), as well as its extension to account for H_2O overlap, using line-by-line radiative transfer calculations, applied to both idealized single columns as well as GCM output. This section details those calculations, and uses them to optimize the parameters κ_0 and l appearing in Eqns. (3) and (7), respectively.

a. Line-by-line calculations

Our idealized single column calculations use the Reference Forward Model (Dudhia 2017) for both line-by-line spectroscopy and radiative transfer, and are very similar to the calculations performed in Jeevanjee and Fueglistaler (2020b). We use HITRAN 2016 spectroscopic data for all available spectral lines of H_2O within 0–1500 cm^{-1} and CO_2 within 500–850 cm^{-1}, for only the most common isotopologue of both gases. We consider highly idealized atmospheric profiles with variable T_s and uniform tropospheric RH, a baseline CO_2 concentration of $q_i = 280$ ppmv, and a constant lapse rate of $\Gamma = 7$ K/km up to to a tropopause at $T_{tp} \equiv 200$ K, with constant, negative stratospheric lapse rate Γ_{strat} above. Specific humidity is uniform in the stratosphere and equal to the tropopause value. For many calculations we will use a 'BASE' column with $T_s = 300$ K, tropospheric RH $= 0.75$, and $\Gamma_{strat} = 0$. We run RFM at a spectral resolution of 0.1 cm^{-1} and on a vertical grid with uniform spacing of 100 m up to model top at 50 km. Calculations include H_2O continuum effects unless otherwise noted, and are parameterized using RFM's implementation of the MT_CKD continuum (Mlawer et al. 2012). Far-wing absorption from CO_2 lines is suppressed using RFM's χ factor (Cousin et al. 1985). Note that we neglect the 1000 cm^{-1} CO_2 band for

the sake of a clean comparison with Eqn. (7), but that for a quadrupling to 1120 ppmv this band can contribute an additional ~ 1 W/m^2 of forcing in a global average, a roughly 10% effect (e.g. Zhao et al. 2018). See Seeley et al. (2020) and Zhong and Haigh (2013) for further analyses of the contributions from additional CO_2 bands, and their effect on the logarithmic scaling of CO_2 forcing.

The 'global' LBL calculations (i.e. parallelized calculations on GCM output) shown below follow those of Paynter and Ramaswamy (2012) at a resolution of 0.01 cm^{-1}, using RFM to produce optical depth profiles and then employing a four-stream solver following the method of Clough et al. (1992).

b. Parameter optimization

To set the parameters l and κ_0 and as a first, idealized test of (7), we calculate the instantaneous TOA forcing $\mathscr{F}_{4x}$ from a quadrupling of CO_2 for our idealized single columns with variable surface temperature T_s, isothermal stratosphere ($\Gamma_{strat} = 0$), and for CO_2 as the only radiatively active species (CO_2-only). The results of this calculation, using both RFM as well as (7), are shown in Fig. 2a for various values of l. The value $l = 10.4$ cm^{-1} minimizes the errors in this comparison and yields an excellent fit, and will be used henceforth. Note that this value is within the $l = 10.4 - 11.5$ cm^{-1} range reported in Seeley et al. (2020); Jeevanjee and Fueglistaler (2020b); Wilson and Gea-Banacloche (2012), and that all values in this range yield a reasonable fit.

Next we optimize κ_0. We do this by considering the same columns as in the previous paragraph but with $T_s = 300$ K and with variable Γ_{strat}. These non-isothermal stratospheres allow us to probe which κ_0 value yields the most appropriate emission pressure p_0 and hence T_{strat} [cf. Eqns. (3),(5)]. A comparison of $\mathscr{F}_{4x}$ as computed by RFM and (7) for these columns and for various values of κ_0 is shown in Fig. 2b. This panel shows that for typical values of $-4 < \Gamma_{strat} < 0$ K/km,

the value $\kappa_0 = 60\ \mathrm{m}^2/\mathrm{kg}$ provides an excellent fit. This is identical to the value obtained via a fit to CO_2 *spectroscopy* (not forcing) in Seeley et al. (2020). Note, however, that large errors appear for larger magnitude Γ_{strat}, showing the limitations of using a single, idealized emission pressure p_0 to represent emission near band center. Also, note that by optimizing l first using $\mathscr{F}_{4\mathrm{x}}$ calculations which are insensitive to κ_0 (due to $\Gamma_{\mathrm{strat}} = 0$), and then optimizing κ_0 using this value of l, we avoid compensating errors in setting these parameter values. These and other parameter values used in this paper are tabulated in Table 1.

4. Geographic distribution of $\mathscr{F}_{4\mathrm{x}}$ with CO_2 only

Now we apply Eqn. (7) along with (5) to more realistic atmospheric columns to obtain a geographical distribution of CO_2 forcing. We continue to consider the CO_2-only case, postponing an analysis of the effects of H_2O overlap to Sections 5 and 6. We will also only consider forcings relative to preindustrial values of q_{i}. For the validity of (7) across a wider range of q_{i}, see Seeley et al. (2020).

We take as atmospheric data a March 22, 1981 snapshot from of a historical run of GFDL's AM3 (Donner et al. 2011). This equinoctal snapshot has meridional temperature gradients typical of the annual mean, but also exhibits zonal variations due to synoptic-scale weather which provides a more stringent test of our simple model than annual mean fields. We calculate the forcing $\mathscr{F}_{4\mathrm{x}}$ from a quadrupling of CO_2 for each column using both our global LBL code as well as Eqn. (7), with the results in Fig. 3a-c. Despite its simplicity, Equation (7) does an excellent job capturing the spatial pattern and overall magnitude of CO_2 forcing as calculated by the global LBL, in both the zonal mean and fully spatially resolved. The most conspicuous error is the overestimate of the zonal mean forcing near 50° N, due to a stratospheric temperature minimum near p_0 which biases our estimate of stratospheric emission.

Several other features of Fig. 3a-c deserve mention. As pointed out in the introduction and also found in previous studies (which typically include H_2O and clouds, e.g. H16, Byrne and Goldblatt 2014; Myhre and Stordal 1997), there is a strong meridional gradient in CO_2 forcing, with large values in the tropics and values close to zero or even negative near the poles. [The potentially surprising negative values[2] over Antarctica were emphasized by Schmithüsen et al. (2015), but subsequently put into context by Smith et al. (2018) and Flanner et al. (2018).[3]] There are also several small-scale regions of enhanced forcing throughout the tropics, as well as a diminished forcing over the Tibetan Plateau.

The simplicity of (7) allows us to identify the origin of these and other spatial variations in $\mathscr{F}_{4x}$. The only variables in (7) are T_s and T_{strat}, which are plotted in Fig. 3d-f. The T_s map is almost identical to the $\mathscr{F}_{4x}$ maps, showing that the spatial variations in $\mathscr{F}_{4x}$ in the CO_2-only case stem almost entirely from T_s, with T_{strat}-variations (only about ± 15 K across the globe) playing a much smaller role. Accordingly, the strong meridional gradient in zonal mean T_s matches that of $\mathscr{F}_{4x}$, while the meridional gradient in T_{strat} is weak. With such weak T_{strat} gradients, both the large-scale meridional gradient in $\mathscr{F}_{4x}$ as well as the regional features mentioned above can then be understood simply as consequences of variations in surface temperature. (In particular, the negative $\mathscr{F}_{4x}$ values over Antarctica occur because there we find $T_s < T_{strat}$.) Physically, surface temperatures are critical because they dictate the strength of the emission blocked by the widened CO_2 band (red lines in Fig. 1a).

5. Theory for $\mathscr{F}_{4x}$ including H_2O overlap

[2]Note that this negative CO_2 forcing is related to, but distinct from, the negative *climatological* greenhouse effect discussed in, e.g., Sejas et al. (2018).

[3]In particular, a negative instantaneous forcing can still lead to a positive surface temperature perturbation, because of stratospheric adjustment as well as surface-troposphere decoupling.

a. Heuristics

We now consider overlap between the 667 cm^{-1} CO_2 band and the H_2O rotational band and continuum. To get a feel for the impact of H_2O overlap, Fig. 4 shows the zonal mean forcing for our GCM snapshot for both the CO_2-only and H_2O overlap cases, as computed with our global LBL code. It is immediately apparent that H_2O overlap significantly modulates the meridional gradient in CO_2 forcing from the CO_2-only case, by significantly reducing $\mathscr{F}_{4\mathrm{x}}$ in the tropics (H_2O overlap makes little difference in the very dry regions poleward of roughly $\pm 65^\circ$). A map of this forcing (Fig. 7a below) also shows zonal asymmetries in tropical $\mathscr{F}_{4\mathrm{x}}$, which appear related to synoptic-scale weather.

To understand this, we must understand how H_2O changes the heuristic picture of CO_2 forcing in Fig. 1. Returning to our idealized single-column calculations, Fig. 5b shows $p_{\mathrm{em}}(\widetilde{\nu})$ as calculated by RFM for $q = 0,\ 280,\ 1120$ ppmv, in our BASE atmospheric column but now in the presence of H_2O. We see that the surface emission from Fig. 1 is replaced by tropospheric emission from H_2O. This should indeed reduce the forcing relative to the CO_2-only case, as increasing CO_2 will now displace H_2O emission from the *atmosphere* rather than displacing warmer surface emission. Furthermore, this displaced H_2O emission will itself depend on relative humidity RH, and so drier areas will exhibit warmer H_2O emission and hence a stronger forcing, thus potentially explaining the meridional gradient and zonal asymmetries in tropical $\mathscr{F}_{4\mathrm{x}}$ seen in Figs. 4 and 7a.

To construct an analog to Fig. 1a, we first assume that the H_2O emission on each side of the CO_2 band has an (RH-dependent) emission temperature (continuing to make the emission level approximation), and that under an increase in CO_2 it is this emission which will be swapped for stratospheric emission. This idealization is depicted in Fig. 5a. We consider the $550 - 600$ cm^{-1} spectral interval to be the the low wavenumber side of the CO_2 band, and quantities averaged over

or pertaining to this interval will be signified with a '-' ; similarly, we consider $750-800$ cm^{-1} as the high wavenumber side, and quantities averaged over or pertaining to this interval will be signified with a '+'.

To turn the heuristic picture of Fig. 5a into a formula which generalizes (7), we will estimate spectrally averaged optical depths $\tau_{\rm est}^{\pm}$, which we can combine with an emission level $\tau^{\rm H_2O}$ to find $T(\tau_{\rm est}^{\pm}=\tau_{\rm em}^{\rm H_2O})$. (Appendix B shows that an appropriate H_2O emission level is $\tau_{\rm em}^{\rm H_2O}=0.6$, which we use henceforth.) Depending on whether or not these temperatures are greater than $T_{\rm s}$ or not, we will then have emission temperatures (Eqn. (B4))

$$T_{\rm em}^{\pm} \equiv \min(T_{\rm s},\, T(\tau_{\rm est}^{\pm}=\tau_{\rm em}^{\rm H_2O}))\,. \tag{8}$$

There is an implicit but strong assumption here that in spectrally averaging Eqn. (B4), we may commute the 'min' function with the spectral averaging. The limitations of this assumption will become evident below. Regardless, with (8) in hand we may then construct a mean H_2O emission temperature

$$\overline{T}_{\rm em} \equiv \frac{T_{\rm em}^{+}+T_{\rm em}^{-}}{2} \tag{9}$$

which can be substituted into (7) for $T_{\rm s}$, in line with the heuristic picture in Fig. 5a.

b. Theory

Now we proceed with the quantitative details. Since optical depth is a vertical integral of absorber mass times absorption coefficient, a prerequisite for calculating $\tau_{\rm est}^{\pm}$ is to obtain estimated, spectrally-averaged H_2O absorption coefficients $\kappa_{\rm est}^{\pm}$. A complication, however, is that $\kappa_{\rm est}^{-}$ is dominated by line absorption, whereas $\kappa_{\rm est}^{+}$ is dominated by continuum absorption (Shine et al. 2012, and Appendix A). Accordingly, we approximate $\kappa_{\rm est}^{-}$ as scaling with foreign pressure broadening

only (Pierrehumbert 2010), whilst κ^+_{est} scales with self-broadening only:

$$\kappa^-_{\text{est}} = \kappa^-_{\text{ref}} \frac{p}{p^-_{\text{ref}}} \tag{10a}$$

$$\kappa^+_{\text{est}} = \kappa^+_{\text{ref}} \frac{\text{RH}}{\text{RH}_{\text{ref}}} e^{(\alpha_0 - \sigma)(T - T^+_{\text{ref}})} \quad . \tag{10b}$$

The reference absorption coefficients $\kappa^\pm_{\text{ref}}$ are evaluated at distinct reference pressures and temperatures $(p^\pm_{\text{ref}}, T^\pm_{\text{ref}})$, and κ^+_{est} also requires a reference relative humidity RH_{ref}. The constant $\alpha_0 \equiv \frac{L}{R_\text{v} T^{+2}_{\text{ref}}}$ results from linearization of Clausius-Clapeyron, and $\sigma = .02\ \text{K}^{-1}$ is an explicit temperature scaling coefficient. Equation (10b) and the parameter values therein are derived in detail and evaluated in Appendix A. Parameter values are recorded in Table 1.

The approximations (10) then allow for an analytical evaluation of $\tau^\pm_{\text{est}}$, as follows. We integrate using temperature as our dummy integration variable, and set the lower bound of the integral to the cold-point tropopause temperature T_{tp} whose H_2O concentrations are assumed negligible (here and below we take the cold-point to demarcate the top of the troposphere). For τ^-_{est}, which we model as being due to line absorption, such a calculation was already performed in Jeevanjee and Fueglistaler (2020b), so we simply quote their Eqn. (12):

$$\tau^-_{\text{est}} = D \kappa^-_{\text{ref}} \frac{p}{p^-_{\text{ref}}} \text{WVP}_0 \exp\left(-\frac{L}{R_\text{v} T}\right) \tag{11a}$$

where $\text{WVP}_0 = \frac{(T_\text{s} + T_{\text{tp}})\text{RH} p^*_v}{2\Gamma L}$ depends on RH and has units of water vapor path, $p^*_v = 2.5 \times 10^{11}$ Pa is a reference value for the saturation vapor pressure p^*_v where $p^*_v(T) = p^*_v \exp(-L/R_\text{v} T)$, and all other symbols have their usual meaning.

For $\tau^+_{\rm est}$, the self-broadening scaling (10b) makes for a different calculation. Denoting vapor density by $\rho_{\rm v}$ (kg/m^3) and noting that $\rho_{\rm v}(T) \approx \rho_{\rm v}(T^+_{\rm ref})\exp(\alpha_0(T-T^+_{\rm ref}))$, we have

$$\begin{aligned}
\tau^+_{\rm est} &= D\int_{T_{\rm tp}}^{T} \kappa^+_{\rm est}\rho_{\rm v}\frac{dT'}{\Gamma} \\
&\approx D\frac{{\rm RH}^2}{{\rm RH}_{\rm ref}}\rho^*_{\rm v}(T^+_{\rm ref})\int_{T_{\rm tp}}^{T}\kappa^+_{\rm ref}e^{\alpha(T'-T^+_{\rm ref})}\frac{dT'}{\Gamma} \quad \text{where } \alpha \equiv 2\alpha_0-\sigma \\
&= D\frac{{\rm RH}^2\rho^*_{\rm v}(T^+_{\rm ref})\kappa^+_{\rm ref}}{{\rm RH}_{\rm ref}\Gamma\alpha}e^{\alpha(T-T^+_{\rm ref})}\,. \qquad (11b)
\end{aligned}$$

Inverting Eqns. (11) at $\tau^\pm_{\rm est} = \tau^{\rm H_2O}_{\rm em}$ then yields

$$T(\tau^-_{\rm est}=\tau^{\rm H_2O}_{\rm em}) = \frac{T^*}{W\left[\frac{T^*}{T^-_{\rm ref}}(D\,{\rm WVP}_0\kappa^-_{\rm ref}/\tau_{\rm em})^{\frac{R_d\Gamma}{g}}\right]} \quad \text{where } T^* \equiv \frac{LR_d\Gamma}{gR_{\rm v}} \qquad (12a)$$

$$T(\tau^+_{\rm est}=\tau^{\rm H_2O}_{\rm em}) = T^+_{\rm ref} + \frac{1}{\alpha}\ln\left(\frac{\tau_{\rm em}\Gamma\alpha{\rm RH}_{\rm ref}}{D{\rm RH}^2\rho^*_{\rm v}(T^+_{\rm ref})\kappa^+_{\rm ref}}\right)\,. \qquad (12b)$$

Note the dependence of $T^+_{\rm em}$ on ${\rm RH}^2$ in (12b), characteristic of the continuum. Equations (12) are the expressions we seek, and will be combined below with Eqns. (8) and (9) to yield a generalization of (7) valid in the presence of H_2O.

c. Validation

We validate the expressions (12) for $T^\pm_{\rm em}$ by comparing them to the spectral average of

$$T_{\rm em}(\widetilde{\nu}) \equiv \min(T_{\rm s}, T(\tau_{\widetilde{\nu}}=\tau_{\rm em})) \qquad (13)$$

as calculated from RFM output for our single-columns with $T_{\rm s}=300$ K, no CO_2, and with varying RH. The ground truth $\int T_{\rm em}(\widetilde{\nu})d\widetilde{\nu}$ for $T^\pm_{\rm em}$ is compared to our estimates (12) in Figure 6a,b, which shows that Eqns. (12) do an excellent job of capturing the variation of $T^-_{\rm em}$ with RH, and do a good job with $T^+_{\rm em}$ down to RH values of 0.025, at which a significant fraction of wavenumbers in the

'+' spectral region become optically thin and thus have $T_{\rm em}(\widetilde{\nu}) = T_{\rm s}$. In this case the min function in (13) does not commute with the spectral averaging, violating the assumption behind (8). This makes our expressions for $T^{\pm}_{\rm em}$ an overestimate whenever the relevant spectral region contains a mix of optically thick and thin wavelengths. This circumstance also occurs at the lower $T_{\rm s}$ typical of the extratropics, as we will see below.

[As an aside, note that the $T(\tau^{\pm}_{\rm est} = \tau_{\rm em})$ in Eqns. (12) are actually *independent* of $T_{\rm s}$, i.e. they are '$T_{\rm s}$-invariant'. Once they are smaller than $T_{\rm s}$, then, the emission to space from their respective spectral regions should also be independent of $T_{\rm s}$. This unique property of H_2O emission temperatures was noted as far back as Simpson (1928), and has far-reaching implications for radiative cooling and precipitation, outgoing longwave radiation, and the water vapor feedback (Jeevanjee and Romps 2018; Jeevanjee 2018; Koll and Cronin 2018; Ingram 2010). There are also implications for CO_2 forcing, which we return to below.]

With some confidence in our expressions (12) for $T^{\pm}_{\rm em}$, we now substitute $\overline{T}_{\rm em}$ from Eqn. (9) into Eqn. (7) to obtain an expression for CO_2 forcing in the presence of H_2O overlap:

$$\mathscr{F} = 2l \ln\left(\frac{q_{\rm f}}{q_{\rm i}}\right)\left[\pi B(\widetilde{\nu}_0, \overline{T}_{\rm em})) - \pi B(\widetilde{\nu}_0, T_{\rm strat})\right] \qquad \text{(w/H}_2\text{O overlap)}. \tag{14}$$

Note that as RH $\to 0$, $\overline{T}_{\rm em} \to T_{\rm s}$ so this equation indeed generalizes (7).

As a preliminary test of (14) we take our single-column, $T_{\rm s} = 300$ K, variable RH calculations (with $q_i = 280$ ppmv) and compare $\mathscr{F}_{4\rm x}$ as calculated from RFM with $\mathscr{F}_{4\rm x}$ calculated from (14) and (12). The result is shown in Fig. 6c and shows quite good agreement between the two, though the errors in $T^{+}_{\rm em}$ at low RH discussed above do lead to small (~ 0.5 W/m^2) errors in $\mathscr{F}_{4\rm x}$.

6. Geographic distribution of $\mathscr{F}_{4x}$ with H_2O overlap

We now estimate $\mathscr{F}_{4x}$ with H_2O overlap for our GCM snapshot using Eqns. (8), (9), (12), and (14), where Γ in Eqns. (12) is diagnosed for each column as a mass-weighted average between the cold-point tropopause and either the surface or the next highest temperature inversion, and RH is diagnosed for each GCM column as the precipitable water in the troposphere divided by its saturation value. The results of this computation are shown in Figure 7b,c, and show that Eqns. (7) and (12) capture the spatial distribution and overall magnitude of $\mathscr{F}_{4x}$ with H_2O overlap almost as well as they do in the CO_2-only case, but with slightly larger errors in the extratropics (which we discuss further below). This supports the heuristic picture of Fig. 5a, i.e. that the effect of H_2O on CO_2 forcing can be thought of as simply a change in the intensity of emission (i.e. the $T_{\rm em}$) blocked by CO_2.

We now return to the T_s-invariance of $T(\tau^{\pm}_{\rm est} = \tau_{\rm em})$ in Eqns. (12). One consequence of this T_s-invariance, in combination with Eqn. (14), is that while CO_2-only forcing (at fixed q_i) grows with increasing T_s (Fig. 2a), forcing with H_2O overlap should asymptote to a constant value of (14) evaluated on the average of the temperatures in Eqns. (12) (assuming fixed RH and $T_{\rm strat}$). We check this in Figure 8, which shows $\mathscr{F}_{4x}$ calculated from both RFM as well as Eqns. (7) and (12), for a series of our idealized atmospheric columns with variable T_s and fixed $q_i = 280$ ppmv and RH $= 0,\ 0.75$. These plots confirm that the presence of H_2O sets an upper bound on $\mathscr{F}_{4x}$ with respect to T_s which is well captured by our simple model.[4] Physically, as T_s increases so does the water vapor path and hence the H_2O optical thickness at all wavenumbers. There is thus a transition in the origin of the emission blocked by an increase in CO_2, from surface emission to emission from H_2O, the latter of which is T_s-invariant. In reality this occurs at different water vapor paths for different wavenumbers, and thus in the spectral integral this transition is smooth

[4] A similar result can also be found in Fig. 14a of Paynter and Ramaswamy (2012).

and begins even at $T_s = 250$ K (Fig. 8a). In our simple model, however, this transition can only occur separately for the '-' and '+' regions (Eqns. (12)) so this transition is more discrete (Fig. 8b). Close comparison of panels a and b of Fig. 8 show that these errors in $\mathscr{F}_{4x}$ with RH $= 0.75$ maximize around $T_s = 260 - 280$ K, temperatures typical of the extratropics where the errors are also most pronounced in Fig. 7. Similar to the RH errors discussed in the previous section, these errors are due to a mix of H_2O and surface emission on either side of the CO_2 band, leading to a breakdown of the assumption behind (8) and an overestimate of the forcing.

The upper bound seen in Fig. 8 is realized beginning at roughly $T_s \approx 300$ K, a typical T_s of the present day tropics. This suggests that the forcing curves in the tropics in Fig. 7c may be thought of as having attained a global maximum (for RH ≈ 0.75), with further local maxima in the subtropics arising only from the low RH values there. Indeed, recalculating $\mathscr{F}_{4x}$ for our GCM snapshot using (14) and (12) but fixing RH=0.7 yields the dashed red curve, which varies very little across the tropics. Tests also show that the zonal asymmetries in Fig. 7 are also due to zonal asymmetries in RH, due to the intrusion of deep tropical moisture filaments into the subtropics (e.g Pierrehumbert and Roca 1998; Pierrehumbert 1998).

It is important to note that this upper bound on CO_2 forcing does *not* imply an upper bound on the total greenhouse effect from CO_2, nor on any resultant warming. Increasing CO_2 will always yield a positive forcing and hence some warming. We are making the much narrower statement that at fixed CO_2 baseline concentration q_i, the *increase* in total CO_2 greenhouse effect from increasing q_i to q_f (i.e the forcing) has a T_s-dependence which asymptotes to an upper bound. But even in the tropics where this upper bound is likely realized, every quadrupling of CO_2 will still instantaneously increase the heat trapped in the Earth system by roughly 7 W/m^2, and that is just in the 667 cm^{-1} band. At higher q_i other spectral regions start to contribute to the forcing, making

this particular upper bound irrelevant and yielding a super-logarithmic scaling of CO_2 forcing with CO_2 concentrations (Seeley et al. 2020; Zhong and Haigh 2013).

7. Summary and Discussion

We summarize our main results as follows:

- Clear-sky CO_2 forcing in the absence of H_2O depends solely on surface-stratosphere temperature contrast [Eqn. (7)] and has a strong meridional gradient, which can be attributed largely to the meridional gradient in surface temperature (Fig. 3).

- The meridional forcing gradient is significantly modulated by the presence of H_2O (Fig. 4), where H_2O replaces surface emission at the edges of the CO_2 band with colder atmospheric emission (Fig. 5).

- The T_s-invariance of H_2O emission temperatures $T_{em}^{\pm}$ implies an upper bound (with respect to T_s variations) on the CO_2 forcing per doubling (Fig. 8). This upper bound is likely realized in the present-day tropics (Fig. 7), but is only relevant for q_i close to preindustrial values, and does not imply a saturation of the total CO_2 greenhouse effect.

The present work could be extended in several ways. One important extension would be towards the calculation of the adjusted rather than instantaneous forcing, as the adjusted forcing has long been recognized to be more directly related to surface warming (e.g. Hansen et al. 1997; Houghton et al. 1994; Rind and Lacis 1993). Our rationale for nonetheless focusing on the simpler, instantaneous TOA forcing here is two-fold. First, the stratospheric adjustment to the TOA forcing is a 30–40% correction (H16 and Zhang and Huang 2014)), which while critical for accurate calculation is not necessary for the basic understanding pursued here. Second, we saw that spatial variations in clear-sky TOA forcing are driven largely by temperature and humidity

variations in the troposphere-surface system, rather than spatial variations in stratospheric temperature; thus stratospheric adjustment is unlikely to contribute significantly to the heterogeneity or state-dependence of CO_2 forcing.

Nevertheless, one could try to extend the formalism presented here to estimate the stratospheric adjustment to the forcing. One route to doing this would be to first evaluate the instantaneous forcing at the tropopause (rather than TOA), using the formalism presented in Appendix B of Seeley et al. (2020). One could then estimate the adjusted forcing as the average of the instantaneous tropopause and TOA forcings, as argued in H16.

Another extension of this work would be to generalize Eqn. (7) to cloudy columns, and hence to compute all-sky forcing. This might be accomplished by simply replacing T_s with a diagnosed cloud-top temperature, just as we replaced T_s by T_{em} in the presence of H_2O. Clouds, like H_2O, should simply change the upwelling radiation which is blocked by additional CO_2. This is already well-known in the literature as the 'cloud-masking' of CO_2 forcing (e.g. H16), but might be succinctly and quantitatively described by the substitution of cloud-top temperature for T_s in (7).

Although this work focuses on the spatial variations of CO_2 forcing, the physics of these variations is simply the atmospheric state-dependence of CO_2 forcing, which also has implications for CO_2 forcing as a function of base climate. For instance, a very cold, Snowball-Earth climate (e.g. Hoffman et al. 2017) will have negligible H_2O and a much smaller surface-stratosphere temperature contrast, which would lead to much reduced CO_2 forcings relative to the present day. This fact and its implications for exiting the Snowball-Earth state were noted by Pierrehumbert (2004), but Eqn. (7) makes this precise and allows for quantitative estimates of this effect. Note that this sensitivity of Eqn. (7) to base climate means that in general one must distinguish between climate sensitivity (response of T_s to given change in TOA flux) and 'carbon sensitivity' (response of T_s to a given CO_2 change, i.e. a doubling). This distinction is also necessitated by the dependence

of CO_2 forcing on base CO_2 concentration, as emphasized in Seeley et al. (2020) and references therein.

The state dependence of CO_2 forcing may also be relevant to the spread in CO_2 forcing amongst GCMs (e.g. Soden et al. 2018; Chung and Soden 2015b,a; Zhang and Huang 2014). This spread is often attributed to parameterization error in GCM broadband radiation schemes, but may also have a contribution from spread in GCM base states. Equation (14) is computationally inexpensive to evaluate and thus might be applied to GCM output to estimate this contribution. Indeed, one can simply differentiate (7) with respect to T_s and evaluate at $T_\mathrm{s} = 288$ K, obtaining $2l(\ln 2)\pi\frac{\partial B}{\partial T}(\widetilde{\nu}_0, 288\text{ K}) = 0.070\text{ W/m}^2\text{/K}$ for CO_2 doubling. Thus, biases of 2-3 K in T_s should bias $\mathscr{F}_{2\mathrm{x}}$ by roughly 0.1-0.2 $\mathrm{W/m^2}$. One can also consider T_strat biases, which by a similar differentiation of (7) but with respect to T_strat and evaluated at $T_\mathrm{strat} = 220$ K yields a sensitivity of 0.04 $\mathrm{W/m^2/K}$. Biases of 4-5 K in T_strat (Butchart et al. 2011) would thus also bias $\mathscr{F}_{2\mathrm{x}}$ by 0.1-0.2 $\mathrm{W/m^2}$.

Finally, it is worth noting that our analytical model can explain empirically-determined features of the linear regression model of H16. For example, $p_0(280\text{ ppmv}) = 16$ hPa from (3) is very close to the empirically determined 10 hPa value used in H16 to evaluate stratospheric temperatures. As another example, consider H16's T_s regression coefficient of 0.066 $\mathrm{W/m^2/K}$ for CO_2 doubling. According to our model, this coefficient should simply be the 0.070 $\mathrm{W/m^2/K}$ calculated in the previous paragraph, a close numerical agreement.

Acknowledgments. NJ thanks Yi Huang for discussions, Robert Pincus and V. Ramaswamy for encouragement, and W. Happer for discussion of CO_2 spectroscopy and for pointing out the Wilson and Gea-Banacloche (2012) reference. NJ was supported by a Harry Hess post-doctoral fellowship

from Princeton Geosciences, JS is supported by a HUCE fellowship, and STF is supported by NSF grants GS-1417659 and AGS-1660538.

APPENDIX A

Estimate for H_2O self-broadened absorption coefficient

This appendix discusses our determination of the spectrally-averaged reference absorption coefficients $\kappa^{\pm}_{\rm ref}$ appearing in (10), and also derives the expression (10b) for the self-broadened absorption coefficient profile $\kappa^{+}_{\rm est}$.

Self-broadened continuum H_2O absorption coefficients experience both an explicit temperature scaling as well as pressure broadening, the latter of which scales linearly with *vapor* pressure $p_{\rm v}$ rather than the dry air pressure p (Pierrehumbert 2010). These scalings are thus relative to a reference temperature and reference vapor pressure, the latter of which can be written in terms of the saturation vapor pressure $p^*_{\rm v}$ and reference RH as $p_{\rm v,ref} = {\rm RH}_{\rm ref} p^*_{\rm v}(T_{\rm ref})$. The vapor pressure scaling can then be written

$$\frac{p_{\rm v}}{p_{\rm v,ref}} \;=\; \frac{{\rm RH} p^*_{\rm v}(T)}{{\rm RH}_{\rm ref} p^*_{\rm v}(T_{\rm ref})} \;\approx\; \frac{\rm RH}{{\rm RH}_{\rm ref}} e^{\alpha_0 (T - T_{\rm ref})} \quad \text{where } \alpha_0 \equiv \tfrac{L}{R_{\rm v} T^2_{\rm ref}} \,.$$

As for the explicit temperature scaling, this takes the form $e^{\sigma(T_{\rm ref} - T)}$ (Mlawer et al. 2012).

Since the '+' wavenumber region is dominated by continuum absorption (as we will see), we will adopt the above vapor pressure scaling for $\kappa^{+}_{\rm est}$, as well as the explicit temperature scaling coefficient $\sigma = .021$ K^{-1} relevant for this wavenumber region (Mlawer et al. 2012). We specify reference values ${\rm RH}_{\rm ref} = 0.75$ and $T^{+}_{\rm ref} = 275$ K for $\kappa^{+}_{\rm est}$, and $(p^{-}_{\rm ref}, T^{-}_{\rm ref}) = (370\,{\rm hPa},\, 245\,{\rm K})$ for $\kappa^{-}_{\rm est}$, which will scale with the dry air pressure [Eqn. (10a)]. In general these reference pressures and temperatures are arbitrary, and are chosen here to minimize errors from our various approximations

(as noted below). We can now write down $\kappa^+_{\rm est}$ as

$$\kappa^+_{\rm est} \;=\; \kappa^+_{\rm ref}\frac{\rm RH}{\rm RH_{ref}}e^{(\alpha_0-\sigma)(T-T^+_{\rm ref})}\;. \tag{A1}$$

This is Eqn. (10b) in the main text. Equation (10a) is standard and can be found in textbooks (e.g. Pierrehumbert 2010), although it neglects temperature scaling of line absorption, an issue to which we return below.

To gauge the accuracy of Eqns. (10), Fig. A1 shows profiles of spectrally-averaged total absorption coefficient $\kappa_{\rm tot}$, lines-only contribution $\kappa_{\rm lines}$, and the difference $\kappa_{\rm ctm}$ which we can ascribe to the continuum, for both the '+' and '-' wavenumber regions. These profiles are calculated via RFM for our BASE column, where $\kappa_{\rm lines}$ is calculating by running RFM without continuum effects, and all spectral averages are performed geometrically rather than arithmetically. Figure 7 shows that for our BASE column the continuum contribution $\kappa_{\rm ctm}$ dominates in the '+' region but not in the '-' region, justifying our use of continuum scalings for the '+' region only. This figure also shows our estimates (10), with $\kappa^\pm_{\rm ref}$ taken to be equal to $\kappa^\pm_{\rm tot}(p^\pm_{\rm ref},T^\pm_{\rm ref},{\rm RH_{ref}})$, yielding $\kappa^-_{\rm ref}=0.1$ m^2/kg and $\kappa^+_{\rm ref}=0.025$ m^2/kg. Our estimates (10) thus agree with $\kappa^\pm_{\rm tot}$ at $(p^\pm_{\rm ref},T^\pm_{\rm ref},{\rm RH_{ref}})$ by construction, but due to the many approximations we have made do not have the same logarithmic slope (i.e. scaling) as $\kappa_{\rm tot}$. However, because H_2O optical depth is an integral of $\kappa_{\rm tot}$ weighted by $p_{\rm v}$, Clausius-Clapeyron scaling means it is only important for $\kappa_{\rm est}$ to have the right order of magnitude in the range of $(T_{\rm em}-20\ {\rm K},T_{\rm em})$ or so, within which our estimates are accurate to roughly a factor of two (by our choice of $T^\pm_{\rm ref}$).

It is interesting to note that the logarithmic slopes of $\kappa_{\rm lines}$ and $\kappa_{\rm ctm}$ are comparable for a given wavenumber range, despite the naive expectation that $\kappa_{\rm lines}$ scales with p (which varies by a factor of 5 over the vertical range shown in Fig. A1) and $\kappa_{\rm ctm}$ scales with $p_{\rm v}$ (which varies by a factor of 700). However, $\kappa_{\rm lines}$ also exhibits a temperature scaling, which we ignore and which

accounts for much of the error in the slope of $\kappa_{\rm est}$ in Fig. A1a. At the same time, $\kappa_{\rm ctm}$ also exhibits a temperature scaling but with opposite sign which *weakens* its C-C scaling [Eqn. (A1)]. These opposing temperature scalings for $\kappa_{\rm lines}$ and $\kappa_{\rm ctm}$ modify our naive expectations, and seem to conspire to produce surprisingly similar overall logarithmic slopes. Whether or not this is a coincidence, or is perhaps related to the hypothesis that continuum absorption is simply due to far-wing line absorption (e.g. Ma et al. 2008), could be investigated further.

APPENDIX B

On the emission level approximation and the choice of $\tau_{\rm em}$

In sections 2 and 5 we made the 'emission level' approximation that emission to space can be regarding as originating from a single level, and in the atmosphere we set these levels as $\tau_{\rm em}^{\rm CO_2} = 0.5$ and $\tau_{\rm em}^{\rm H_2O} = 0.6$. This appendix discusses this approximation, and justifies these choices of $\tau_{\rm em}$ for our applications in particular. Other values of $\tau_{\rm em}$ may be required for other greenhouse gases and other applications.

It will be convenient to use the framework and notation of Jeevanjee and Fueglistaler (2020a), i.e. we consider a gray gas with idealized optical depth, temperature, and source function profiles

$$\tau = \tau_s \left(\frac{p}{p_s}\right)^{\beta}, \quad T = T_{\rm s}\left(\frac{p}{p_s}\right)^{R_d\Gamma/g}, \quad B = B_s\left(\frac{T}{T_{\rm s}}\right)^{\alpha}$$

where subscript "s" denotes the surface value of a quantity and B has units of $\mathrm{W/m^2}$. These profiles combine to yield

$$B(\tau) = B_s\left(\frac{\tau}{\tau_s}\right)^{\gamma} \qquad \text{where} \tag{B1}$$

$$\gamma \equiv \frac{d\ln B}{d\ln\tau} = \alpha\frac{R_d\Gamma}{g}\frac{1}{\beta}\,. \tag{B2}$$

Now, the emission level (EL) approximation simply says that

$$\text{OLR} \approx \begin{cases} B_s & \text{if } \tau_s < \tau_{\text{em}} \\ B(\tau_{\text{em}}) & \text{if } \tau_s \geq \tau_{\text{em}} \end{cases} \qquad \text{(EL approx.)} \tag{B3}$$

for some 'emission level optical depth' τ_{em} which may depend on the parameters introduced above. This τ_{em} may be thought of as characterizing the transition between surface and atmospheric emission, or equivalently between 'optically thin' and 'optically thick' regimes. As such, we expect $\tau_{\text{em}} \sim O(1)$ (Jeevanjee and Fueglistaler 2020b; Petty 2006; Wallace and Hobbs 2006), as we will indeed find below. Note that in terms of an effective emission temperature T_{em} which satisfies $\text{OLR} \approx B(T_{\text{em}})$, the EL approximation can be rewritten as

$$T_{\text{em}} \;=\; \min(T_{\text{s}}, T(\tau_{\text{em}})) \; . \tag{B4}$$

To determine τ_{em}, we first analytically compute the OLR for our idealized gray gas, using Eqn. (B1) and assuming $\tau_s \gg 1$:

$$\begin{aligned} \text{OLR} &= \int_0^\infty B_s (\tau/\tau_s)^\gamma e^{-\tau} d\tau \\ &= \frac{B_s}{\tau_s^\gamma} \widetilde{\Gamma}(1+\gamma) \end{aligned} \tag{B5}$$

where $\widetilde{\Gamma}(\gamma+1)$ denotes Euler's Gamma function evaluated at $\gamma+1$, and the tilde is introduced to distinguish it from the atmospheric lapse rate. We may then combine Eqns. (B1), (B3), and (B5) and solve for τ_{em}, obtaining

$$\tau_{\text{em}} \;=\; \left[\widetilde{\Gamma}(1+\gamma)\right]^{1/\gamma} \; . \tag{B6}$$

A plot of this curve is shown in Fig. 7. To determine τ_{em}, then, we simply need appropriate values for γ for CO_2 and H_2O emission. For CO_2, τ_{em} only enters our theory quantitatively in determining $p_0(q)$ (Eqn. 3), which lies in the stratosphere where $\Gamma \approx -2$ K/km. Using this value for Γ and also setting $\beta = 2$ [Eqn. (2)] and $\alpha = 4$ (Jeevanjee and Fueglistaler 2020a), Eqn. (B2) then yields $\gamma^{CO_2} = -0.1$. Plugging this into (B6) yields $\tau_{\text{em}}^{CO_2} \approx 0.5$.

For H_2O, we are interested in tropospheric emission ($\Gamma \approx 7$ K/km) in the neighborhood of the CO_2 band ($\alpha = 4$). Jeevanjee and Fueglistaler (2020b) found $\beta = 5.5$ for line absorption,[5] thus yielding $\gamma^{H_2O} = 0.15$ and hence $\tau_{em}^{H_2O} = 0.6$.

It is interesting to note that the γ parameter of Eqn. (B2) was also found by Jeevanjee and Fueglistaler (2020a) to determine the validity of the cooling-to-space approximation, which was found to hold when $\gamma \ll 1$. It is also interesting to note that in this limit, we may Taylor-expand the $\widetilde{\Gamma}$ function in (B6) and invoke the fact that the $\frac{d\widetilde{\Gamma}(x)}{dx}|_{x=1} = -\gamma_{\text{Euler}}$, where γ_{Euler} is the Euler-Mascheroni constant (yet another gamma). A little calculation then shows

$$\lim_{\gamma \to 0} \tau_{\text{em}} = e^{-\gamma_{\text{Euler}}} = 0.56 \, . \tag{B7}$$

This gives a canonical value for τ_{em} appropriate for circumstances where $|\gamma| \ll 1$, and indeed this value is very close to both our $\tau_{em}^{CO_2}$ and $\tau_{em}^{H_2O}$.

References

Butchart, N., and Coauthors, 2011: Multimodel climate and variability of the stratosphere. *Journal of Geophysical Research Atmospheres*, **116 (5)**, 1–21.

Byrne, B., and C. Goldblatt, 2014: Radiative forcing at high concentrations of well-mixed greenhouse gases. *Geophysical Research Letters*, **41 (1)**, 152–160.

Chung, E.-S., and B. J. Soden, 2015a: An Assessment of Direct Radiative Forcing, Radiative Adjustments, and Radiative Feedbacks in Coupled OceanAtmosphere Models*. *Journal of Climate*, **28 (10)**, 4152–4170.

[5] A β value appropriate for continuum absorption can be read off from Eqn. (13) of Jeevanjee and Fueglistaler (2020b) by doubling the contribution from Clausius-Clapeyron scaling due to the quadratic dependence of continuum absorption on vapor pressure, which roughly doubles β to 10. This halves γ^{H_2O} to 0.08, but yields negligible changes in $\tau_{em}^{H_2O}$ (Fig. 7).

Chung, E. S., and B. J. Soden, 2015b: An assessment of methods for computing radiative forcing in climate models. *Environmental Research Letters*, **10 (7)**, 74 004.

Clough, S. A., M. J. Iacono, and J.-l. Moncet, 1992: Line-by-line calculations of atmospheric fluxes and cooling rates: Application to water vapor. *Journal of Geophysical Research*, **97 (D14)**, 15 761.

Coakley Jr., J. A., and P. Yang, 2014: *Atmospheric Radiation: A Primer with Illustrative Solutions*. Wiley-VCH, 239 pp.

Cousin, C., R. L. Doucen, C. Boulet, and a. Henry, 1985: Temperature dependence of the absorption in the region beyond the 4.3-microm band head of CO(2) . 2: N(2) and O(2) broadening. *Applied optics*, **24 (22)**, 3899–3907.

Donner, L. J., and Coauthors, 2011: The dynamical core, physical parameterizations, and basic simulation characteristics of the atmospheric component AM3 of the GFDL global coupled model CM3. *Journal of Climate*, **24 (13)**, 3484–3519.

Dudhia, A., 2017: The Reference Forward Model (RFM). *Journal of Quantitative Spectroscopy and Radiative Transfer*, **186**, 243–253.

Flanner, M. G., X. Huang, X. Chen, and G. Krinner, 2018: Climate Response to Negative Greenhouse Gas Radiative Forcing in Polar Winter. *Geophysical Research Letters*, **45 (4)**, 1997–2004.

Forster, P. M., and Coauthors, 2011: Evaluation of radiation scheme performance within chemistry climate models. *Journal of Geophysical Research Atmospheres*, **116 (D10)**.

Govindasamy, B., and K. Caldeira, 2000: Geoengineering Earth's radiation balance to mitigate CO2-induced climate change. *Geophysical Research Letters*, **27 (14)**, 2141–2144.

Hansen, J., M. Sato, and R. Ruedy, 1997: Radiative forcing and climate response. *Journal of Geophysical Research Atmospheres*, **102 (D6)**, 6831–6864.

Hoffman, P. F., and Coauthors, 2017: Snowball Earth climate dynamics and Cryogenian geology-geobiology. *Science Advances*, **3 (11)**, e1600 983.

Houghton, J. T., L. Meira Filho, J. Bruce, H. Lee, B. Callander, E. Haites, N. Harris, and K. Maskell, Eds., 1994: *Climate change 1994: radiative forcing of climate change and an evaluation of the IPCC 1992 IS92 emission scenarios.* Cambridge University Press, Cambridge, UK, 1–345 pp.

Houghton, J. T. J. T., 2002: *The physics of atmospheres*. Cambridge University Press, 320 pp.

Huang, Y., X. Tan, and Y. Xia, 2016: Inhomogeneous radiative forcing of homogeneous greenhouse gases. *Journal of Geophysical Research*, **121 (6)**, 2780–2789.

Ingram, W. J., 2010: A very simple model for the water vapour feedback on climate change. *Quarterly Journal of the Royal Meteorological Society*, **136 (646)**, 30–40.

Jeevanjee, N., 2018: The physics of climate change: simple models in climate science. *arxiv preprint, http://arxiv.org/abs/1804.09326*, 1802.02695.

Jeevanjee, N., and S. Fueglistaler, 2020a: On the Cooling-to-Space Approximation. *Journal of the Atmospheric Sciences*, **77 (2)**, 465–478.

Jeevanjee, N., and S. Fueglistaler, 2020b: Simple Spectral Models for Atmospheric Radiative Cooling. *Journal of the Atmospheric Sciences*, **77 (2)**, 479–497.

Jeevanjee, N., and D. M. Romps, 2018: Mean precipitation change from a deepening troposphere. *Proceedings of the National Academy of Sciences*, **115 (45)**, 11 465–11 470.

Kiehl, J. T., and B. P. Briegleb, 1993: The relative roles of sulfate aerosols and greenhouse gases. *Science*, **260 (5106)**, 311–314.

Koll, D. D., and T. W. Cronin, 2018: Earth's outgoing longwave radiation linear due to H2O greenhouse effect. *Proceedings of the National Academy of Sciences of the United States of America*, **115 (41)**, 10 293–10 298.

Ma, Q., R. H. Tipping, and C. Leforestier, 2008: Temperature dependences of mechanisms responsible for the water-vapor continuum absorption. I. Far wings of allowed lines. *Journal of Chemical Physics*, **128 (12)**, 0–17.

Merlis, T. M., 2015: Direct weakening of tropical circulations from masked CO2 radiative forcing. *Proceedings of the National Academy of Sciences*, **112 (43)**, 13 167–13 171.

Mlawer, E. J., V. H. Payne, J.-L. Moncet, J. S. Delamere, M. J. Alvarado, and D. C. Tobin, 2012: Development and recent evaluation of the MT_CKD model of continuum absorption. *Philosophical Transactions of the Royal Society A: Mathematical, Physical and Engineering Sciences*, **370 (1968)**, 2520–2556.

Mlynczak, M. G., and Coauthors, 2016: The spectroscopic foundation of radiative forcing of climate by carbon dioxide. *Geophysical Research Letters*, **43**, 5318–5325.

Myhre, G., E. J. Highwood, K. P. Shine, and F. Stordal, 1998: New estimates of radiative forcing due to well mixed greenhouse gases. *Geophysical Research Letters*, **25 (14)**, 2715–2718.

Myhre, G., and F. Stordal, 1997: Role of spatial and temporal variations in the computation of radiative forcing and GWP. *Journal of Geophysical Research: Atmospheres*, **102 (D10)**, 11 181–11 200.

599 Oreopoulos, L., and Coauthors, 2012: The Continual Intercomparison of Radiation Codes: Results
600 from Phase i. *Journal of Geophysical Research Atmospheres*, **117 (6)**, 1–19.

601 Paynter, D., and V. Ramaswamy, 2012: Variations in water vapor continuum radiative transfer
602 with atmospheric conditions. *Journal of Geophysical Research Atmospheres*, **117 (16)**, 1–23.

603 Petty, G. W., 2006: *A First Course in Atmospheric Radiation (2nd Ed.)*. Sundog Pub, 472 pp.

604 Pierrehumbert, R. T., 1998: Lateral mixing as a source of subtropical water vapor. *Geophysical*
605 *Research Letters*, **25 (2)**, 151.

606 Pierrehumbert, R. T., 2004: High levels of atmospheric carbon dioxide necesarry for the termina-
607 tion of global glaciation. *Nature*, **429 (June)**, 646–649.

608 Pierrehumbert, R. T., 2010: *Principles of Planetary Climate*. Cambridge University Press, Cam-
609 bridge, UK.

610 Pierrehumbert, R. T., and R. Roca, 1998: Evidence for control of atlantic subtropical humidity by
611 large scale advection. *Geophysical Research Letters*, **25 (24)**, 4537–4540.

612 Pincus, R., and Coauthors, 2015: Radiative flux and forcing parameterization error in aerosol-free
613 clear skies. *Geophysical Research Letters*, **42 (13)**, 5485–5492.

614 Ramaswamy, V., and Coauthors, 2001: ”Radiative forcing of climate change”. In Climate change
615 2001: the scientific basis’. Tech. rep., IPCC Working Group I, Third Assessment Report, 349–
616 416 pp.

617 Rind, D., and A. Lacis, 1993: The role of the stratosphere in climate change. *Surveys in Geo-*
618 *physics*, **14 (2)**, 133–165.

Schmithüsen, H., J. Notholt, G. König-Langlo, P. Lemke, and T. Jung, 2015: How increasing CO2leads to an increased negative greenhouse effect in Antarctica. *Geophysical Research Letters*, **42 (23)**, 10 422–10 428.

Seeley, J. T., N. Jeevanjee, J. Edman, and D. Romps, 2020: On the logarithmic scaling of CO2 forcing. *Submitted to J Climate*.

Sejas, S. A., M. Cai, G. Liu, P. C. Taylor, and K.-k. Tung, 2016: A Lagrangian view of longwave radiative fluxes for understanding the direct heating response to a CO2 increase. *Journal of Geophysical Research: Atmospheres*, **121**, 1–24.

Sejas, S. A., P. C. Taylor, and M. Cai, 2018: Unmasking the negative greenhouse effect over the Antarctic Plateau. *npj Climate and Atmospheric Science*, **1 (1)**, 17.

Shine, K. P., and P. M. F. Forster, 1999: The effect of human activity on radiative forcing of climate change: A review of recent developments. *Global and Planetary Change*, **20 (4)**, 205–225.

Shine, K. P., I. V. Ptashnik, and G. Rädel, 2012: The Water Vapour Continuum: Brief History and Recent Developments. *Surveys in Geophysics*, **33 (3-4)**, 535–555.

Simpson, G., 1928: Some Studies in Terrestrial Radiation. *Memoirs of the Royal Meteorological Society*, **2 (16)**, 69–95.

Smith, K. L., G. Chiodo, M. Previdi, and L. M. Polvani, 2018: No surface cooling over Antarctica from the negative greenhouse effect associated with instantaneous quadrupling of CO2 concentrations. *Journal of Climate*, **31 (1)**, 317–323.

Soden, B. J., W. D. Collins, and D. R. Feldman, 2018: Reducing uncertainties in climate models. *Science*, **361 (6400)**, 326–327.

Stuber, N., R. Sausen, and M. Ponater, 2001: Stratosphere adjusted radiative forcing calculations in a comprehensive climate model. *Theoretical and Applied Climatology*, **68 (3-4)**, 125–135.

Thomas, G. E., and K. Stamnes, 2002: *Radiative Transfer in the Atmosphere and Ocean*. Cambridge University Press, Cambridge, UK, 517 pp.

Wallace, J. M., and P. V. Hobbs, 2006: *Atmospheric Science: An Introductory Survey*. Academic Press, 504 pp.

Wilson, D. J., and J. Gea-Banacloche, 2012: Simple model to estimate the contribution of atmospheric CO2 to the Earth's greenhouse effect. *American Journal of Physics*, **80 (4)**, 306.

Zhang, M., and Y. Huang, 2014: Radiative Forcing of Quadrupling CO2. *Journal of Climate*, **27 (7)**, 2496–2508.

Zhao, M., and Coauthors, 2018: The GFDL Global Atmosphere and Land Model AM4.0/LM4.0: 2. Model Description, Sensitivity Studies, and Tuning Strategies. *Journal of Advances in Modeling Earth Systems*, 735–769.

Zhong, W., and J. D. Haigh, 2013: The greenhouse effect and carbon dioxide. *Weather*, **68 (4)**, 100–105.

LIST OF TABLES

Description	Symbol, value	Section described
Wavenumber at band maximum	$\widetilde{\nu}_0 = 667.5\ \mathrm{cm}^{-1}$	Section 2
Reference T and p for CO_2 abs. coefficients	$(T_{\mathrm{ref}}, p_{\mathrm{ref}}) = (250\ \mathrm{K},\ 100\ \mathrm{hPa})$	Section 2
Band-maximum reference CO_2 abs. coefficient	$\kappa_0 = 60\ \mathrm{m}^2/\mathrm{kg}$	Section 3b
Spectroscopic decay parameter	$l = 10.4\ \mathrm{cm}^{-1}$	Section 3b
Emission levels	$\tau_{\mathrm{em}}^{\mathrm{CO_2}} = 0.5, \quad \tau_{\mathrm{em}}^{\mathrm{H_2O}} = 0.6$	Appendix B
Reference T and p for H_2O abs. coefficients (different for '+' and '-' wavenumber regions)	$(T_{\mathrm{ref}}^-, p_{\mathrm{ref}}^-) = (245\ \mathrm{K},\ 370\ \mathrm{hPa})$ $(T_{\mathrm{ref}}^+, p_{\mathrm{ref}}^+) = (275\ \mathrm{K},\ 650\ \mathrm{hPa})$	Appendix A
Reference RH for cont. absorption in '+' region	$\mathrm{RH}_{\mathrm{ref}} = 0.75$	Appendix A
Reference H_2O abs. coefficients	$\kappa_{\mathrm{ref}}^- = 0.1\ \mathrm{m}^2/\mathrm{kg}$ $\kappa_{\mathrm{ref}}^+ = 0.025\ \mathrm{m}^2/\mathrm{kg}$	Appendix A
Clausius-Clapeyron scaling coefficient in '+' region	$\alpha_0 = \frac{L}{R_{\mathrm{v}} T_{\mathrm{ref}}^{+2}}$	Appendix A
Continuum T-scaling for κ_{est}^+	$\sigma = 0.021\ \mathrm{K}^{-1}$	Appendix A
T-scaling for τ_{est}^+	$\alpha = 2\alpha_0 - \sigma$	Appendix A

TABLE 1. Parameters for the simple model of CO_2 forcing. See referenced sections for details.

LIST OF FIGURES

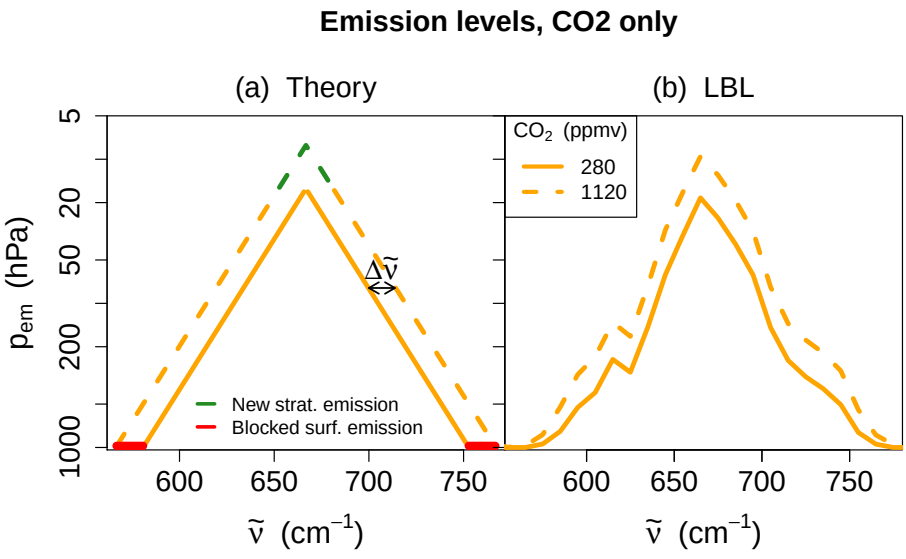

719 FIG. 1. **(a)** Graph of CO_2 emission levels $p_{\rm em}(\widetilde{\nu})$ as given by (3) for $q_{\rm i} = 280$ ppmv and $q_{\rm f} = 4q_{\rm i}$. **(b)** As in (a),
720 but from RFM calculations with CO_2 only for our BASE atmosphere. RFM emission levels are diagnosed by
721 the condition $\tau_{\widetilde{\nu}} = \tau_{\rm em}^{\rm CO_2} = 0.5$ (Appendix B), and are geometrically averaged over 10 $\rm cm^{-1}$ bins. The idealized
722 triangles in (a) are good first order approximations to $p_{\rm em}(\widetilde{\nu})$ as calculated by RFM in (b). In (a), the green
723 dashed lines at top depict the negative stratospheric contribution to the forcing, the orange lines depict the null
724 tropospheric contribution to the forcing, and the red solid lines at bottom depict the positive surface contribution.
725 Equation (7) quantifies these contributions.

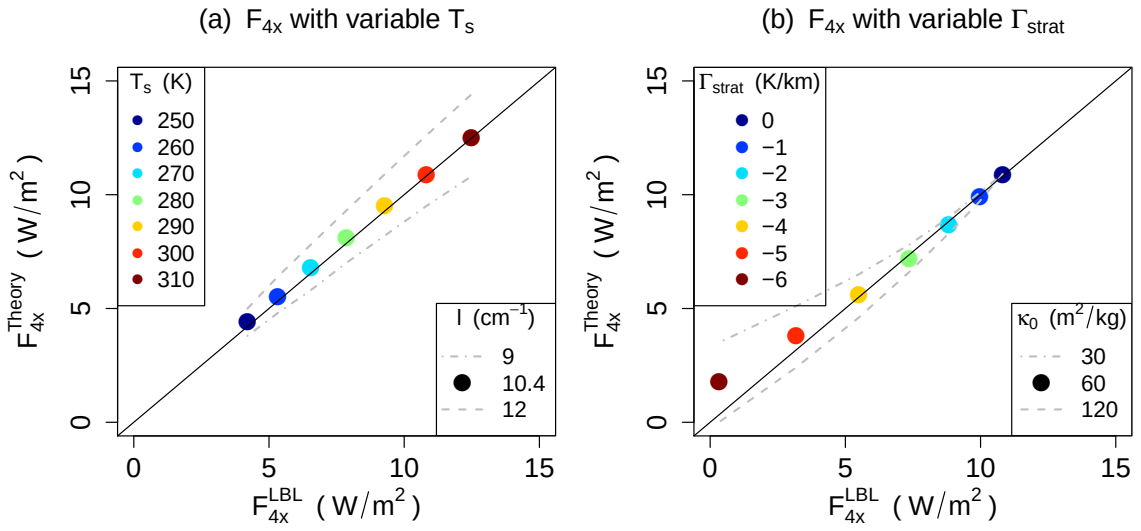

FIG. 2. Comparison of (7) vs. RFM for our idealized, CO_2-only single columns with **(a)** variable T_s and $\Gamma_{strat} = 0$ and **(b)** $T_s = 300$ K and variable Γ_{strat}. Optimization of l in panel (a) yields $l = 10.4$ cm^{-1}, and optimization of κ_0 in (b) for $-4 < \Gamma_{strat} < 0$ K/km yields $\kappa_0 = 60$ m^2/kg. With these parameter values, the good fit in these panels across a range of T_s and Γ_{strat} provide a first validation of (7).

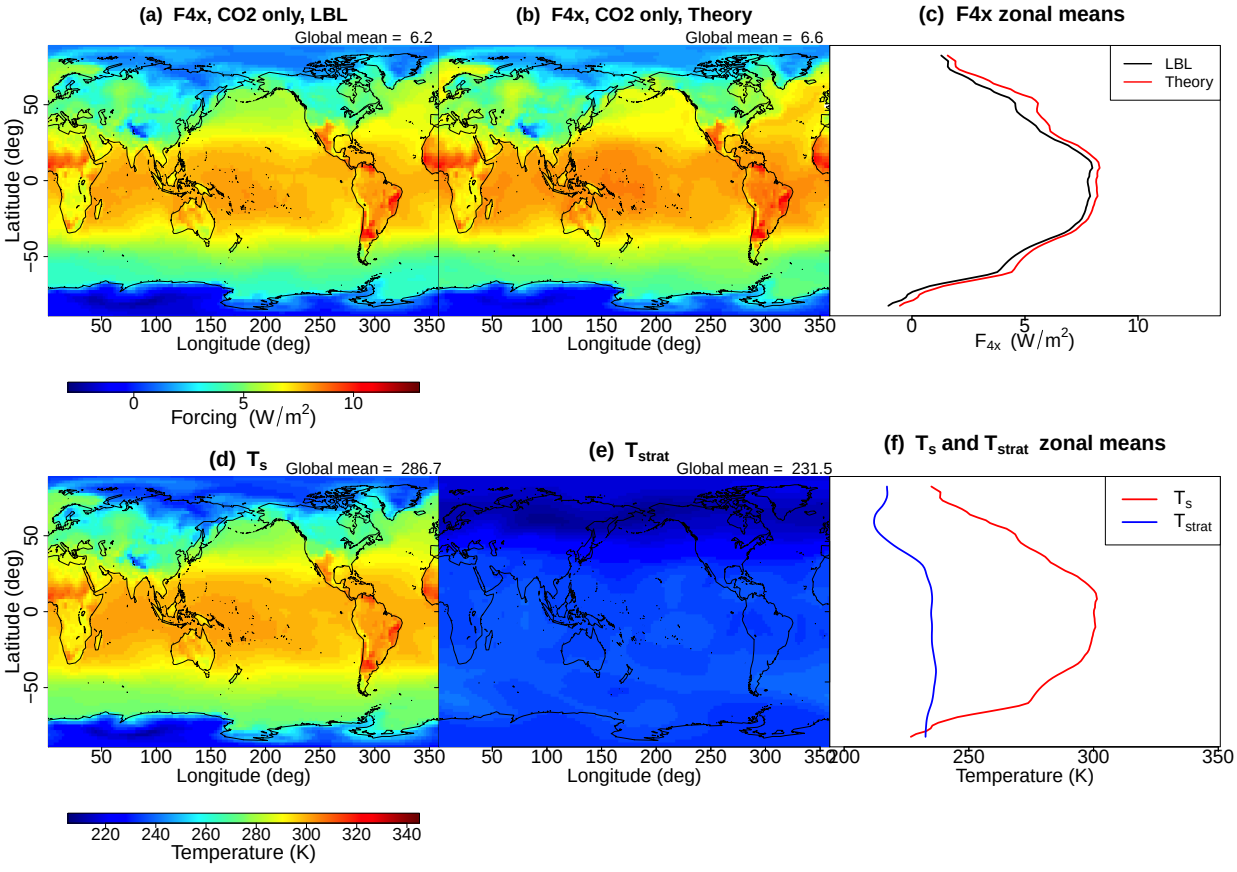

730 FIG. 3. Maps of **(a)** CO_2 forcing $\mathscr{F}_{4x}$ with CO_2 only from a LBL calculation with RFM **(b)** as in (a), but using
731 the simple model (7) **(d)** surface temperature T_s **(e)** stratospheric emission temperature T_{strat}, as diagnosed by
732 (5). Panel **(c)** shows zonal means of (a)-(b), and **(f)** shows zonal means of (d)-(e). The spatial variations in CO_2
733 forcing, and in particular the meridional gradient, are captured by the simple model. Furthermore, the T_s map
734 in (d) is almost identical to the $\mathscr{F}_{4x}$ maps in (a)-(b), showing that the spatial variations in $\mathscr{F}_{4x}$ in the CO_2-only
735 case stem almost entirely from T_s, with T_{strat}-variations playing a much smaller role. Accordingly, the strong
736 meridional gradient in zonal mean T_s matches that of $\mathscr{F}_{4x}$ [panels (c) and (f)], while the meridional gradient in
737 T_{strat} is weak.

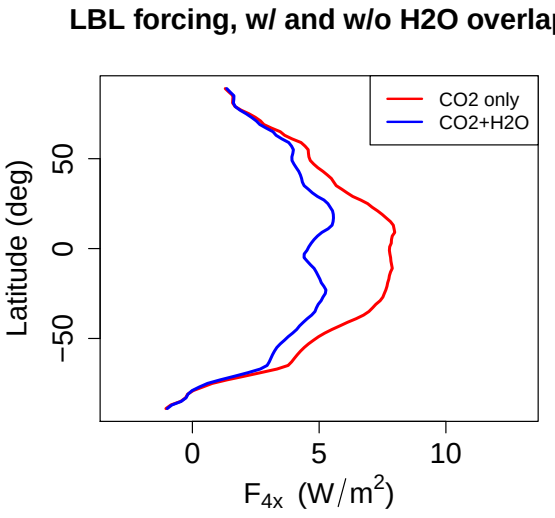

738 FIG. 4. Zonal mean forcing for our GCM snapshot for both the CO_2-only and H_2O overlap cases, as computed
739 with our global LBL code. H_2O strongly modulates the CO_2 forcing outside the dry polar regions, thus also
740 modulating the meridional gradient in CO_2 forcing.

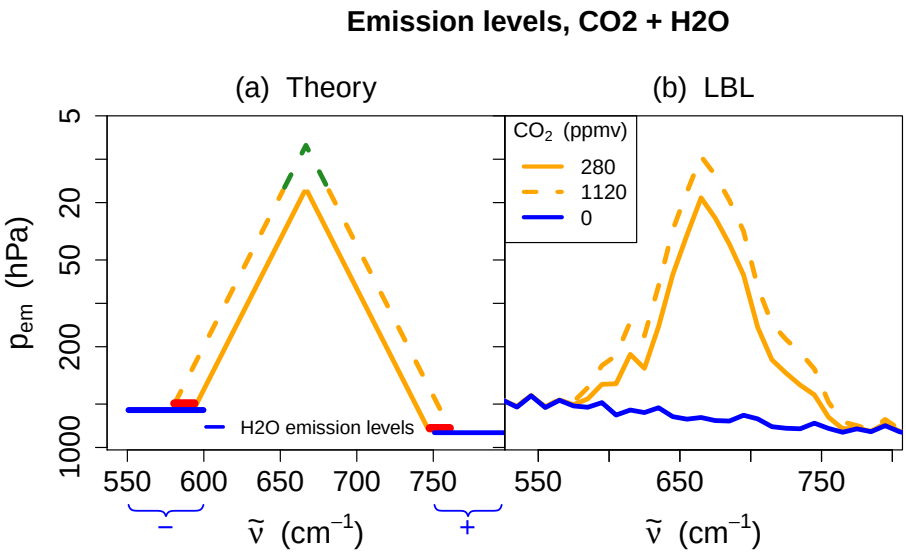

741 FIG. 5. As in Fig. 1 but with H_2O overlap, again for the BASE atmosphere. H_2O emission levels are shown in
742 blue, and in panel (a) are given by Eqns. (12), while in panel (b) are diagnosed directly from RFM by $\tau_{\tilde{\nu}} = 0.5$
743 and geometrically averaged over 10 cm^{-1} bins, just as for CO_2. Panel (b) shows that the presence of H_2O implies
744 that increasing CO_2 blocks tropospheric H_2O emission rather than surface emission. This is idealized in panel
745 (a), which assumes a single emission level in each of two spectral regions, denoted '-' and '+', and spanning the
746 wavenumber ranges $550-600$ cm^{-1} and $750-800$ cm^{-1} respectively.

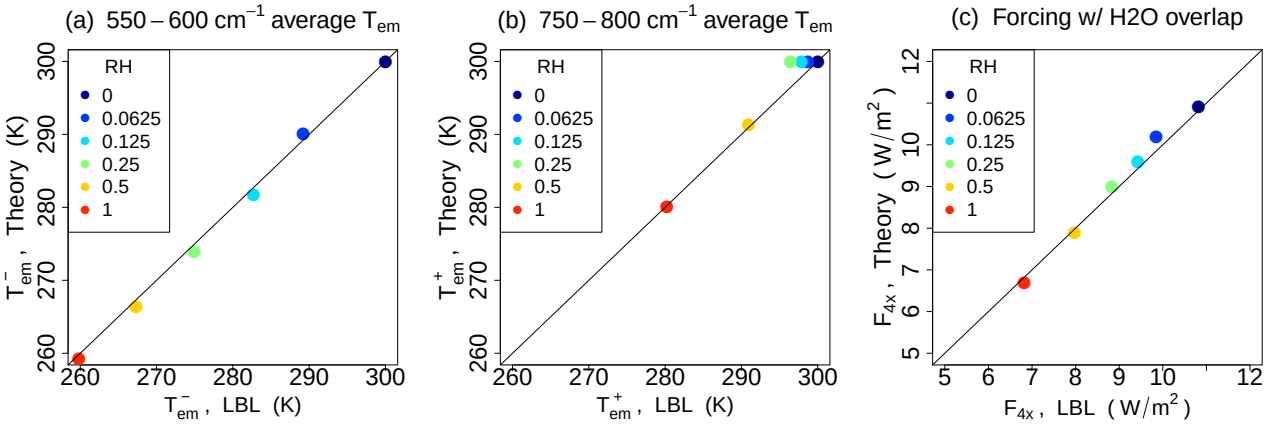

747 FIG. 6. **(a,b)** Validation of our simple expressions (12) for band-averaged H_2O emission temperatures $T^{\pm}_{\rm em}$,
748 as compared to band-averaged $T(\tau_{\tilde{\nu}} = \tau_{\rm em})$ using $\tau_{\tilde{\nu}}$ as output by RFM. This comparison is made for idealized
749 atmospheric columns with $T_{\rm s} = 300$, no CO_2, and varying RH. **(c)** Validation of the simple model of Eqns. (12)
750 and (7) for $\mathscr{F}_{4\rm x}$ in the presence of H_2O, as compared to $\mathscr{F}_{4\rm x}$ calculated by RFM. This comparison is made for
751 idealized atmospheric columns with $T_{\rm s} = 300$, $q_i = 280$ ppmv, and varying RH. The simple expressions (12)
752 predict $T^{\pm}_{\rm em}$ very well except at low RH in the '+' region, leading to small (~ 0.5 W/m^2) errors in $\mathscr{F}_{4\rm x}$ at these
753 RH values.

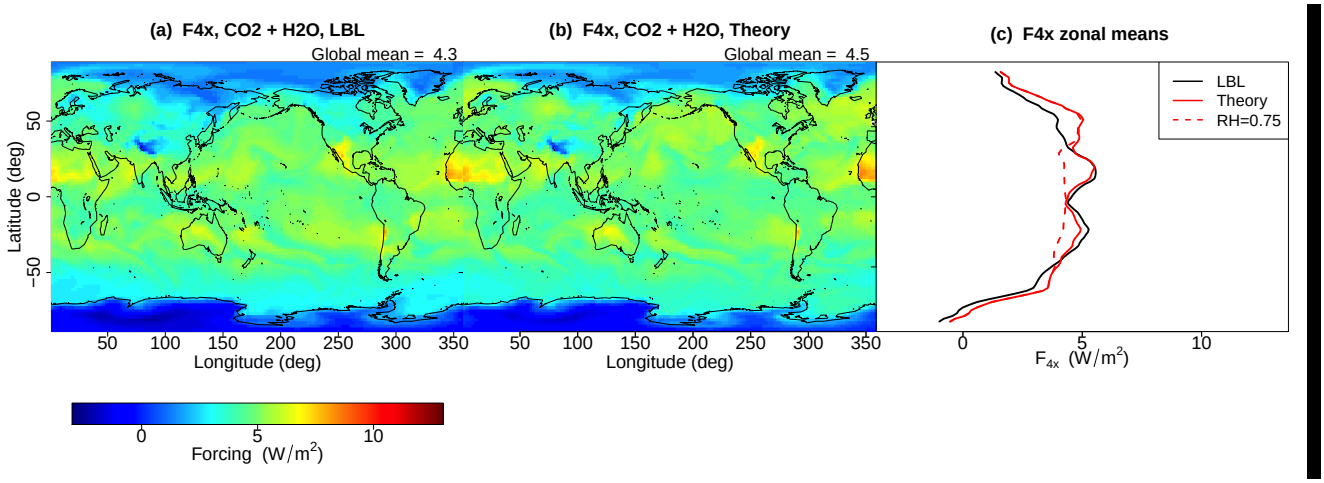

754 FIG. 7. As in Fig. 3a-c, but now including H_2O overlap, where panel (b) is generated using Eqn. (14). By
755 replacing warm surface emission with colder tropospheric emission, H_2O strongly modulates the CO_2 forcing
756 outside the dry polar regions. Spatial variations in $\mathscr{F}_{4x}$ within the tropics due to strong RH variations can also
757 be seen. These features are emulated by the simple model.

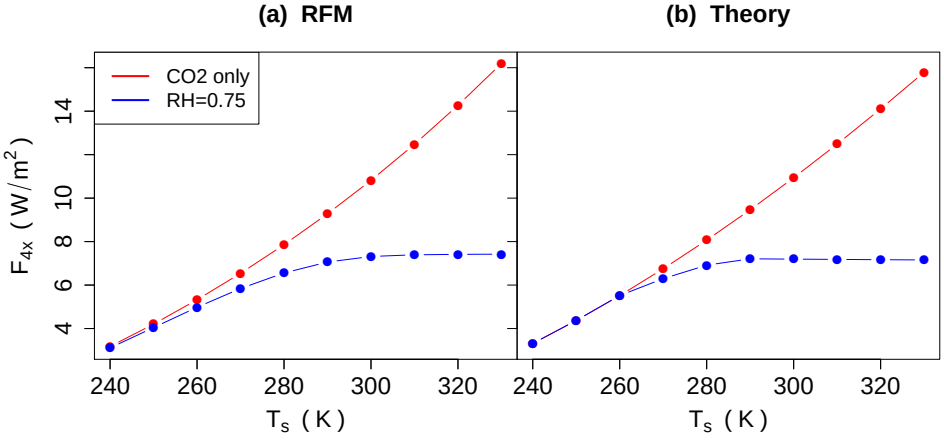

FIG. 8. CO_2 forcing $\mathscr{F}_{4x}$ for our idealized atmospheric columns with varying T_s and all other parameters fixed at the BASE values, in both the absence (red) and presence (blue) of H_2O, from **(a)** RFM and **(b)** our simple model, Equation (14). The presence of H_2O sets an upper bound on $\mathscr{F}_{4x}(T_s)$ (with respect to T_s variations and at fixed baseline CO_2) which does not exist in the CO_2-only case. These behaviors are well captured by our simple model.

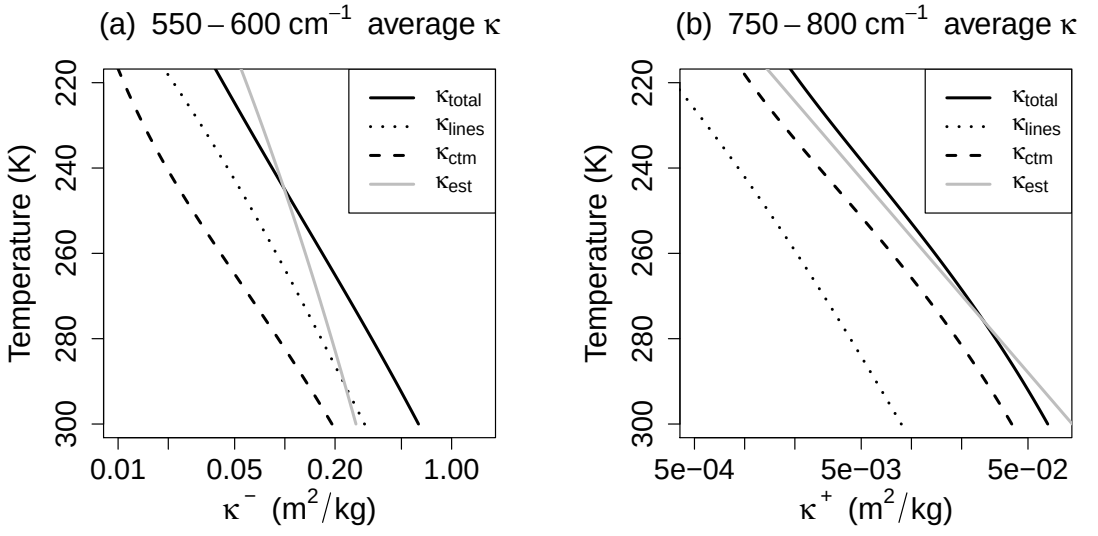

Fig. A1. Profiles of various contributions to spectrally-averaged H_2O absorption coefficients in our BASE column for the wavenumber regions **(a)** 525-625 cm^{-1}and **(b)** 725-825 cm^{-1}. The profiles of $\kappa_{\rm tot}$, $\kappa_{\rm lines}$, and $\kappa_{\rm ctm}$ are calculated with RFM, whereas $\kappa_{\rm est}$ is given by Eqns. (10) with $(\kappa^-_{\rm ref}, \kappa^+_{\rm ref})$ set to $(\kappa^-_{\rm tot}(T^-_{\rm ref}), \kappa^+_{\rm tot}(T^+_{\rm ref}))$, and where $(T^-_{\rm ref}, T^+_{\rm ref}) = (245, 275)$ K. The $\kappa^-_{\rm est}$ profile is a poor approximation to $\kappa^-_{\rm tot}$ far from $T^-_{\rm ref}$ due to our neglect of temperature scaling of line absorption, but is acceptably close within 20 K or so of $T^-_{\rm ref}$. The horizontal axis in both panels is logarithmic, with the same geometric range (of 150) in each.

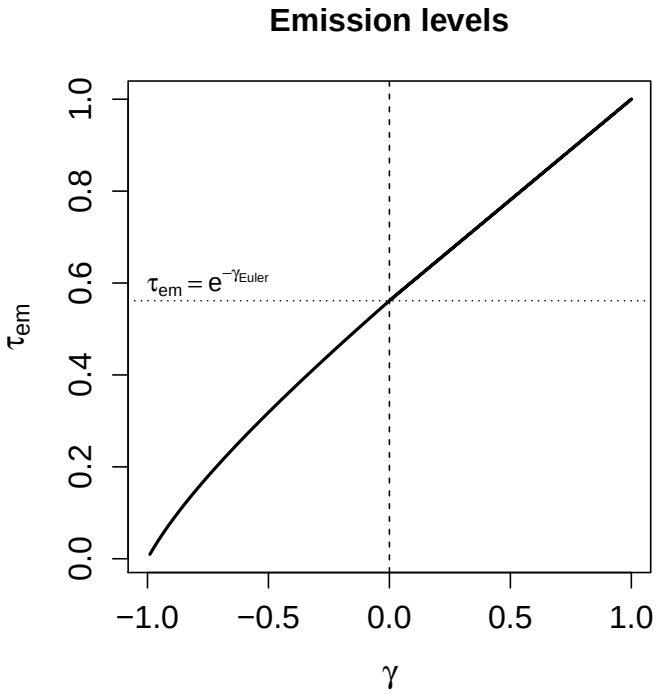

Fig. B1. Plot of Eqn. (B6) for emission levels $\tau_{\rm em}$ as a function of the parameter γ defined in (B2). At $\gamma = 0$, $\tau_{\rm em} = e^{-\gamma_{\rm Euler}} \approx 0.56$, giving a canonical value for $\tau_{\rm em}$ which is indeed close to our value for $\tau_{\rm em}^{\rm CO_2}$ and $\tau_{\rm em}^{\rm H_2O}$.